Science Bulletin 65 (2020) 1743–1751

Contents lists available at ScienceDirect

Science Bulletin

journal homepage: www.elsevier.com/locate/scib

Science Bulletin
www.scibull.com

Article

Evolution of Zn(II) single atom catalyst sites during the pyrolysis-induced transformation of ZIF-8 to N-doped carbons

Qing Wang [a], Toshiaki Ina [b], Wan-Ting Chen [a], Lu Shang [c], Fanfei Sun [d], Shanghai Wei [e], Dongxiao Sun-Waterhouse [a], Shane G. Telfer [f], Tierui Zhang [c], Geoffrey I.N. Waterhouse [a,*]

[a] School of Chemical Sciences, The University of Auckland, Auckland 1142, New Zealand
[b] Research & Utilization Division, Japan Synchrotron Radiation Research Institute, Kouto 679-5148, Japan
[c] Key Laboratory of Photochemical Conversion and Optoelectronic Materials, Technical Institute of Physics and Chemistry, Chinese Academy of Sciences, Beijing 100190, China
[d] Shanghai Synchrotron Radiation Facility, Shanghai Institute of Applied Physics, Chinese Academy of Sciences, Shanghai 201204, China
[e] Department of Chemical and Materials Engineering, Faculty of Engineering, The University of Auckland, Auckland 1142, New Zealand
[f] MacDiarmid Institute for Advanced Materials and Nanotechnology, Massey University, Palmerston North 4442, New Zealand

ARTICLE INFO

Article history:
Received 25 April 2020
Received in revised form 20 May 2020
Accepted 8 June 2020
Available online 16 June 2020

Keywords:
Metal single atom catalysts
Porphyrin-like sites
N-doped carbon
Metal organic frameworks
X-ray absorption spectroscopy

ABSTRACT

The pyrolysis of zeolitic imidazolate frameworks (ZIFs) is becoming a popular approach for the synthesis of catalysts comprising porphyrin-like metal single atom catalysts (SACs) on N-doped carbons (M-N-C). Understanding the structural evolution of M-N-C as a function of ZIF pyrolysis temperature is important for realizing high performance catalysts. Herein, we report a detailed investigation of the evolution of Zn single atom catalyst sites during the pyrolysis of ZIF-8 at temperatures ranging from 500 to 900 °C. Results from Zn L-edge and Zn K-edge X-ray absorption spectroscopy studies reveal that tetrahedral ZnN_4 centers in ZIF-8 transform to porphyrin-like ZnN_4 centers supported on N-doped carbon at temperatures as low as 600 °C. As the pyrolysis temperature increased in the range 600–900 °C, the Zn atoms moved closer to the N_4 coordination plane. This subtle geometry change in the ZnN_4 sites alters the electron density on the Zn atoms (formally Zn^{2+}), strongly impacting the catalytic performance for the peroxidase-like decomposition of H_2O_2. The catalyst obtained at 800 °C (Zn-N-C-800) offered the best performance for H_2O_2 decomposition. This work provides valuable new insights about the evolution of porphyrin-like single metal sites on N-doped carbons from ZIF precursors and the factors influencing SAC activity.

1. Introduction

Carbon supported metal single atom catalysts (SACs) are finding increasing applications in electrocatalysis and chemical energy conversion owing to their high activities and near 100% metal atom utilization [1,2]. The central metal atom in SACs can be coordinated by a variety of electron donors, including N [3], O [4], C [5], S [6], P [7] and combinations thereof. M-N-C SACs (where M is a first, second or third row transition metal) are generally accessed by the co-pyrolysis of precursors rich in the desired metal, nitrogen, and carbon. Commonly used approaches include the adsorption of metal complexes with N-donor ligands onto a porous carbon support followed by a pyrolysis step, or alternatively the pyrolysis of metal coordination polymers or metal organic frameworks rich in nitrogen and carbon, such as zeolitic imidazolate frameworks (ZIFs) [8–10]. However, pyrolysis syntheses make it difficult to achieve a high dispersion of single metal atom sites, owing to the tendency of the metals to aggregate into nanoparticles at the high temperatures (>700 °C). Further, using such pyrolysis routes, it is experimentally difficult to regulate the central metal coordination in SACs, including both the metal coordination number and the coordination neighbours. This lack of control originates from the fact that the precursor carbonization and metal single atom site evolution occur simultaneously during high temperature pyrolysis treatments. Catalytic studies using metal SACs have shown that the activity is strongly dependent on the local metal coordination [11,12]. Thus, understanding the pyrolysis process in detail, including both the evolution of the metal single atom sites and changes to the support with temperature, is essential for the tailoring and optimization of catalyst performance.

In the development of carbon-supported metal SACs, the pyrolysis temperature has a great influence on the local metal coordination of the final carbon products. Experimental evidence suggests

* Corresponding author.
E-mail address: g.waterhouse@auckland.ac.nz (G.I.N. Waterhouse).

https://doi.org/10.1016/j.scib.2020.06.020
2095-9273/

that MN_4 sites on N-doped carbons are thermodynamically stable, and indeed favoured relative to nanoparticles at temperatures above 800 °C when metal loadings are low (a few atom percent) [13–15]. For example, Wang et al. [16] tracked the Co species formed during the pyrolysis of bimetallic Zn,Co-doped ZIF crystals using extended X-ray absorption fine structure (EXAFS) analyses. The Co nodes in Zn,Co-doped ZIF transformed into Co clusters at lower temperatures (600–800 °C) upon heating under N_2, followed by Co atom migration into porphyrin-like CoN_4 sites at higher temperatures. Using environmental transmission electron microscopy, Wei et al. [17,18] visualized the transformation of noble metal nanoparticles (Pd, Pt, Au) into single metal atoms on a N-doped carbon support at temperatures above 900 °C. These studies indicate that for certain metals, nitrogen coordinated single metal sites are favored over metal clusters during pyrolysis processes or heat treatments at high temperatures. Recently, *in-situ* X-ray absorption spectroscopy (XAS) was used to characterise the change in coordination of N-doped carbon supported iron as a function of pyrolysis temperature. Fe(II) salts were adsorbed onto a N-doped carbon support at room temperature, after which the resulting composites were heated in N_2 to high temperatures [19,20]. At temperatures below 300 °C, Fe oxides formed, transforming to a tetrahedral FeO_4 coordination motif at temperatures up to 600 °C, then finally to an in-plane FeN_4 coordination at temperatures above 600 °C. In contrast, the pyrolysis of SiO_2 supported Fe(II) salts led to the formation of metallic Fe nanoparticles. The study highlighted the importance of the N-doped carbon support for achieving a high dispersion of metal single sites at high temperatures.

Zeolitic imidazolate framework 8 (ZIF-8) is a porous metal organic framework (MOF) consisting of Zn^{2+} nodes tetrahedrally coordinated by four nitrogen atoms from 2-methylimidazole linkers. Owing to its high surface area and porosity, along with high carbon and nitrogen content (molecular formula $ZnC_8H_{10}N_4$, 42.2 wt% C, 24.6 wt% N), ZIF-8 crystals are frequently used as precursors in the synthesis of N-doped carbon materials by high temperature pyrolysis [21–25]. Typical pyrolysis temperatures are above 800 °C, at which temperatures most of the Zn is reduced to the zerovalent state and evaporates (the boiling point of Zn is 907 °C). Post ZIF-8 crystal synthesis, the Zn^{2+} nodes can be replaced by other transition metal cations, thus offering precursors for the pyrolysis-based synthesis of a wide range of porphyrin-like M-N-C materials (M = Fe [26], Co [16], Ni [27], Mn [28], Cr [29], Cu [30], Ru [31], Ir [32], Pt, Pd, Au [17]). However, it remains elusive how porphyrin-like single metal sites are formed during the pyrolysis of ZIF-8 precursors.

Herein, we report results of a detailed investigation of the local Zn coordination during pyrolysis of ZIF-8 crystals at temperatures between 500 and 900 °C under a N_2 atmosphere. X-ray diffraction (XRD), X-ray photoelectron spectroscopy (XPS), Zn L-edge and Zn K-edge XAS, and Zn K-edge EXAFS were used to characterize the pyrolysis products formed at each temperature (denoted herein as Zn-N-C-*T*, where *T* is the pyrolysis temperature in degrees Celsius). The analyses revealed the formation of porphyrin-like ZnN_4 sites at temperatures as low as 600 °C, with the Zn^{2+} centers moving into the N_4 plane at elevated temperatures (>800 °C). This shift into the N_4 plane slightly modifies the electronic properties of the Zn atoms due to the influence of π-conjugated carbon basal plane associated with microcrystalline graphite domains formed at high temperatures. The net result is that Zn-N-C-800 showed excellent performance for peroxidase like decomposition of H_2O_2 into hydroxyl radicals (·OH), highlighting the sensitivity of the catalytic properties of Zn single atom catalysts to the local Zn coordination. Results guide the development of improved metal single atom catalysts for both catalytic and electrocatalytic processes.

2. Experimental

2.1. Materials

Zinc nitrate hexahydrate (99%), 2-methylimidazole (98%), 3,3′,5,5′-tetramethylbenzidine (98%), 5,10,15,20-tetraphenyl-21H, 23H-porphine zinc (ZnTPP), and sodium acetate (99%), were purchased from Sigma-Aldrich. All other chemicals and solvents used were of reagent grade and used without further purification. Milli-Q water (18.2 MΩ) was used throughout this work.

2.2. Syntheses

2.2.1. Synthesis of ZIF-8

$Zn(NO_3)_2{\cdot}6H_2O$ (3.36 g) was dissolved in 40 mL of methanol. This solution was then added rapidly to a solution of 2-methylimidazole (8 g) in 120 mL of methanol under constant stirring. The resulting solution was then stirred for 1 h at room temperature, after which the stirring was discontinued and the reaction mixture left at room temperature for 24 h. The ZIF-8 product was collected by centrifugation, washed three times with methanol, then finally oven dried at 60 °C for 12 h.

2.2.2. Synthesis of Zn-N-C-T

ZIF-8 (1 g) was pyrolyzed under flowing N_2 for 2 h at the following temperatures: 500, 600, 700, 750, 800, or 900 °C. The heating rate was 5 °C min^{-1}. The pyrolysis products were subsequently treated in 0.5 mol L^{-1} H_2SO_4 at 80 °C for 8 h to remove any Zn nanoparticles, then washed repeatedly with water and ethanol. The obtained zinc-containing N-doped carbons are denoted herein as Zn-N-C-*T*, where *T* is the pyrolysis temperature in degrees Celsius.

2.3. Characterization

High resolution transmission electron microscopy (HRTEM) images and high-angle annular dark field scanning TEM (HAADF-STEM) images were collected on a FEI TECNAI 20 transmission electron microscope operating at 200 kV. Aberration-corrected HADDF-STEM images and energy-dispersive X-ray spectroscopy (EDX) spectra were acquired on a JEM-ARM300F S/STEM (JEOL) at an operating voltage of 300 kV. Powder XRD patterns were obtained on a Bruker D8 Focus X-ray diffractometer equipped with a Cu Kα radiation source (λ = 1.5405 Å). Diffraction patterns were collected over the 2θ range 5°–70°. Raman spectra were collected on Renishaw inVia Reflex spectrometer system, equipped with a 520 nm laser excitation source. N_2 physisorption measurements were performed on a Micromeritics Tristar 3000 instrument at liquid nitrogen temperature (−196 °C). Inductively coupled plasma-optical emission spectroscopy (ICP-OES, Varian 710) was used to quantify the amount of Zn in the samples. To prepare the samples for ICP-OES, samples (20 mg) were first calcined at 600 °C for 3 h. The calcined samples were then immersed in 10 wt% HNO_3 to liberate any Zn^{2+}, with the samples finally being diluted to the correct ppm range for ICP-OES measurements. XPS data were collected on a Kratos Axis UltraDLD X-ray photo-electron spectrometer, equipped with a monochromatized Al-Kα X-ray source (1486.69 eV). XPS peak fitting was performed using the XPSPEAK4.1 program. Shirley type backgrounds were fitted to the spectra for peak fitting. The C 1s signal of neutral adventitious hydrocarbons (284.5 eV) was used for binding energy scale calibration.

2.4. Synchrotron characterization studies

Zn L-edge, C K-edge and N K-edge X-ray absorption spectra were collected on the soft X-ray spectroscopy beamline at the

Australian Synchrotron. For the analyses, the samples were deposited onto double-sided carbon tape. The XAS data were taken in the total electron yield (TEY) mode at an analysis chamber pressure of ~1×10^{-10} Torr. The TEY data were normalized against a current measured simultaneously on a gold mesh in the beamline to eliminate potential spectral artifacts caused by fluctuations in the beam intensity whilst scanning. The measurements were carried out in high-resolution (HR) mode by increasing the photon energies in steps of 0.05 or 0.1 eV.

Zn K-edge XAS data were collected in transmission mode on the BL01B1 beamline of the Japan Synchrotron Radiation Research Institute (SPring-8, Japan). The storage ring was operated at 8 GeV and a ring current of 44–65 mA. A Si(1 1 1) single crystal was used to monochromatize the X-ray beam, and two ion chambers filled with Ar and N_2 were used as detectors of I_0 and I, respectively. The XAFS raw data were processed with background-subtraction, normalization and Fourier transformation by the standard procedures with Athena module of the IFEFFIT software packages. EXAFS fitting was performed by the Artemis module, following the EXAFS equation below:

$$\chi(k) = \sum_j \frac{N_j S_0^2 F_j(k)}{kR_j^2} \exp\left[-2k^2\sigma_j^2\right] \exp\left[\frac{-2R_j}{\lambda(k)}\right] \sin\left[2kR_j + \varnothing_j(k)\right],$$

where S_0^2 is the amplitude reduction factor, $F_j(k)$ is the effective curved-wave backscattering amplitude, N_j is the number of neighbors in the j_{th} atomic shell, R_j is the distance between the X-ray absorbing central atom and the atoms in the j_{th} atomic shell, λ is the mean free path in Å, $\phi_j(k)$ is the phase shift, σ_j^2 is the Debye-Waller parameter of the j_{th} atomic shell (variation of distances around the average R_j).

2.5. Peroxidase-like activity tests

The peroxidase-like activity tests were conducted in a 0.1 mol L^{-1} sodium acetate buffer solution (pH 3) at room temperature. Typically, 10 μL of a 3,3',5,5'-tetramethylbenzidine solution (TMB in dimethyl sulfoxide, 10 mg mL^{-1}), 50 μL H_2O_2 (30 wt%) and 10 μL of a catalyst dispersion (5 mg mL^{-1}) were added into sodium acetate buffer to give a solution of 1 mL total volume. After 30 min, the time-course evolution of the blue TMB oxidation product was followed spectrophotometrically by monitoring the absorbance at 652 nm using a Shimadzu UV-2600 spectrophotometer.

Further kinetic experiments were conducted using Zn-N-C-800 and different concentrations of the TMB substrate. The experimental procedure was similar to that described above, where 1 mL testing solution contains 5 μL of a Zn-N-C-800 dispersion (5 mg mL^{-1}), 50 μL of H_2O_2 (30 wt%), and varying the amount of the TMB solution (10 mg mL^{-1}) used (1, 2.5, 5, 7.5, 10, 12.5, 15, or 20 μL). The reaction time was 10 min.

Kinetic experiments were also carried out to study the effect of the H_2O_2 concentration, again using Zn-N-C-800 as the catalyst. The experimental procedure was similar to that described above, using 5 μL of a Zn-N-C-800 dispersion (5 mg mL^{-1}), 10 μL of TMB solution (10 mg mL^{-1}), and different amounts of 30% H_2O_2 (5, 10, 25, 50, 75, 100, 150, or 200 μL). The reaction time was 10 min. The Michaelis–Menten constant was calculated according to the Michaelis–Menten saturation curve by GraphPad Prism 6.02 Software.

The effects of pH and temperature on the peroxidase-like activity of Zn-N-C-800 were also studied in the pH range 2.5–10 and at temperatures from 22 to 70 °C. The effect of catalyst loading was studied by varying the amounts of catalyst dispersion (5 mg mL^{-1}) added into the reaction system (from 0, 2.5, 5, to 10 μL), at a fixed reaction time of 10 min. For these tests, all other experimental parameters were the same as those used in the standard peroxidase-like activity test described above.

3. Results and discussion

ZIF-8 crystals were synthesized according to a literature method [23]. The synthesis yielded characteristic truncated rhombic dodecahedral crystals of size ~150 nm (Fig. 1). The ZIF-8 crystals were then pyrolyzed at temperatures ranging from 500 to 900 °C in N_2 for 2 h. Following the pyrolysis step, the solid products were treated in 0.5 mol L^{-1} H_2SO_4 at 80 °C for 8 h to remove any Zn nanoparticles, then washed repeatedly with water and ethanol. The obtained products are denoted here as ZIF-80-500 and Zn-N-C-*T* (*T* = 600, 700, 750, 800, 900 °C). ZIF-8 is thermally stable up to 500 °C. XRD showed that the decomposition of ZIF-8 to a Zn-N-C phase occurred ~600 °C (Fig. S1 online). This was evidenced by the complete disappearance of the sharp ZIF-8 peaks and the emergence of new broad peaks at 26° and 44°, corresponding to the (0 0 2) and (1 0 1) planes of nanocrystalline graphitic carbon (Fig. S1 online). No Zn-related peaks were observed in the XRD patterns.

The absence of Zn nanoparticles in any of the Zn-N-C-*T* materials was verified by HRTEM images and high-angle annular dark field scanning TEM (HAADF-STEM) (Fig. 1), with all of the Zn-N-C-*T* samples inheriting the truncated rhombic dodecahedral morphology of the ZIF-8 precursor. EDX mapping (Fig. S2 online) of Zn-N-C-800 verified a uniform dispersion of Zn, N and C. The aberration-corrected HAADF-STEM image of Zn-N-C-800 (Fig. 2a) showed obvious bright dots (highlighted by red circles), indicating the atomic dispersion of Zn atoms over the N-doped carbon support.

The presence of zinc single atom sites, rather than Zn nanoparticles, in all the Zn-N-C-*T* samples was further confirmed by the absence of a Zn-Zn scattering path in the Fourier transformed Zn K-edge EXAFS spectra for the samples (Fig. 2b). The Zn K-edge R-space plots for the Zn-N-C-*T* samples show two pronounced peaks at 1.6 and 2.6 Å, which by comparison with the data for 5,10,15,20-tetraphenyl-21H,23H-porphine zinc (ZnTPP) can readily be assigned to the first Zn-N shell and second Zn-C shell, respectively. Inductively coupled plasma optical emission spectrometry (ICP-OES, Table S1 online) determined that the Zn contents in the Zn-N-C-*T* samples prepared at 600–900 °C were (3.01–6.53) wt% (following the acid digestion of any ZnO or Zn nanoparticles). The nitrogen content of the Zn-N-C-*T* samples decreased with increasing temperature, though the Zn-N-C-900 sample still possessed a high nitrogen content (13.42 wt%). It should be noted that the pyrolysis of ZIF-8 at 900 °C is now a widely used approach for the preparation of N-doped carbons rich in pyridinic sites for electrocatalytic applications. Most researchers assume that Zn (in the form of metallic Zn) will be fully removed by evaporation at such high temperatures, leaving metal-free N-doped carbon products. However, in this work significant amounts of Zn remained in the Zn-N-C-900 sample (4.67 wt%), which can be attributed to the formation of stable Zn(II) single atom sites early in the pyrolysis process. The heating rate and pressure (atmospheric) used here were likely important parameters for realizing Zn-N-C-*T* products rich in Zn(II) single atom sites at 900 °C. Alternative pyrolysis conditions (faster heating under vacuum, longer pyrolysis time) may have simply yielded an N-doped carbon product.

To gain deeper insights about the valence states of the Zn on going from ZIF-8 to the Zn-N-C-*T* samples, Zn 2p XPS and Zn L-edge XAS analyses were conducted. The two methods are complementary, with XPS probing the occupied states and XAS unoccupied states of Zn atoms. The Zn 2p XPS spectra for ZIF-8 and Zn-N-C-*T* samples (Fig. S3 online) contain two peaks centered

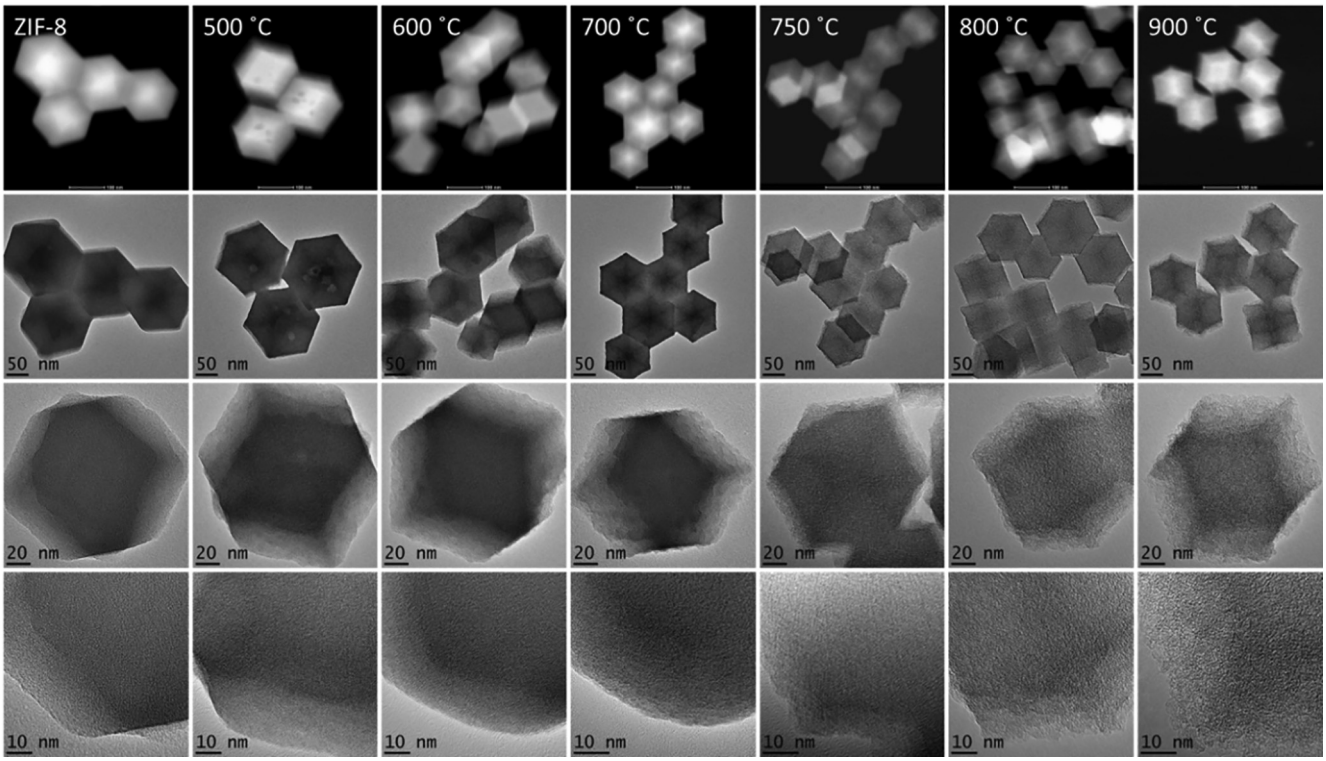

Fig. 1. HAADF-STEM (top) and bright field TEM images for ZIF-8 and its derived Zn-N-C-*T* pyrolysis products.

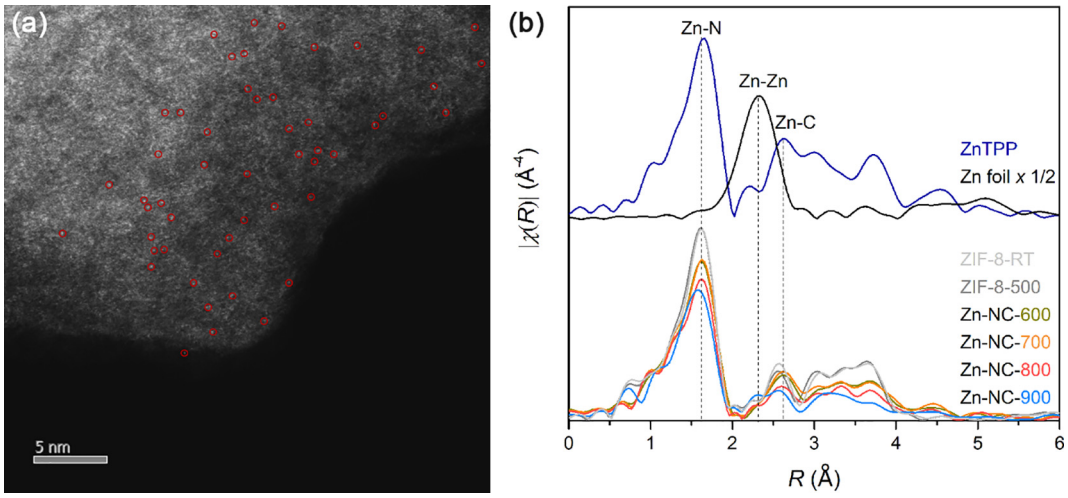

Fig. 2. (Color online) (a) Aberration-corrected HAADF-STEM image of Zn-N-C-800 and (b) Fourier transform of Zn K-edge EXAFS spectra for ZIF-8, various Zn-N-C-*T* samples, and selected reference materials.

at 1021.4 and 1044.3 eV in a 2:1 area ratio, which can readily be assigned to Zn $2p_{3/2}$ and Zn $2p_{1/2}$ signals, respectively, of Zn^{2+}. Zn L-edge XAS (Fig. 3a) provided further confirmation about the oxidation state of Zn and the zinc coordination environment. Zn^{2+} has the $3d^{10}$ electron configuration. ZnTPP belongs to the D_{4h} point group, with a square planar nitrogen ligand field around Zn^{2+} (occupation state $d^2_{b1g}d^2_{a1g}d^4_{eg}d^2_{b2g}$). The spectrum collected for ZnTPP agreed well with reported Zn L-edge spectra for the compound, showing characteristic L_3 and L_2 features around 1024.8 and 1047.8 eV, respectively [33]. These features are associated with the excitation of Zn 2p electrons into π* orbitals of the TPP ligand. The Zn L-edge features that lie ~6 eV higher in photon energy than the main L_3 and L_2 signals are associated with Zn 2p excitations into unoccupied 4 s and 4d states [33]. The Zn L-edge spectra for the Zn-N-C-*T* (*T* = 600–900 °C) samples were almost identical to that collected for ZnTPP, suggesting that the samples contained a near square planar Zn(II) coordination environment similar to that of ZnTPP (Fig. S4 online). The Zn L-edge XAS spectrum for ZIF-8, containing tetrahedral ZnN_4 moieties, was quite distinct from that of ZnTPP and the Zn-N-C-*T* (*T* = 600–900 °C) samples, highlighting the significant difference between their Zn^{2+} coordination environments. The Zn L-edge spectrum for the ZIF-8-500 sample was qualitatively similar to that collected for ZIF-8, consistent to their similar XRD patterns. Clearly, at the low pyrolysis temperature of

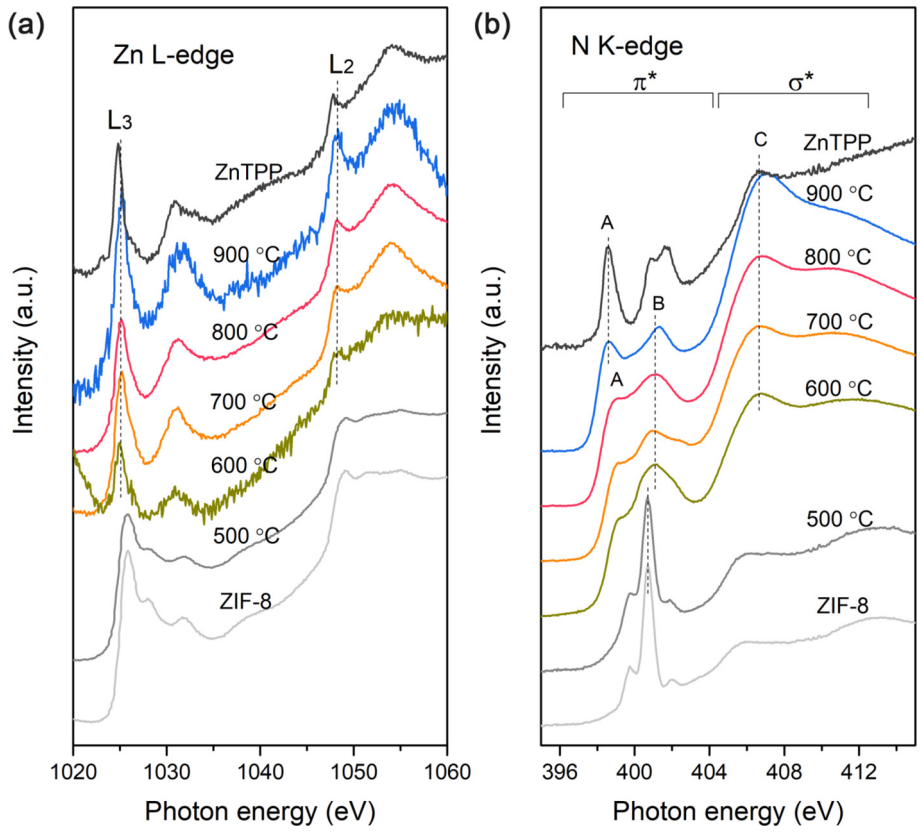

Fig. 3. (Color online) (a) Zn L-edge XAS spectra and (b) N K-edge XAS spectra for ZIF-8 and various Zn-N-C-*T* samples.

500 °C, the Zn^{2+} retains a tetrahedral nitrogen coordination rather than adopting the near square planar nitrogen coordination typical of the Zn-N-C-*T* samples prepared at 600 °C and above.

N K-edge XAS measurements revealed a similar evolution in structure with pyrolysis temperature (Fig. 3b). The N K-edge spectra of ZIF-8 and ZIF-8-500 were similar, dominated by an intense signal around 400.7 eV, which can readily be attributed to the excitation of a N 1s electron from the pyrrolic N of 2-methylimidazole into an antibonding π* orbital of the same ligand. The weaker feature around 406 eV is due to a N 1s → σ* transition. The N K-edge XAS spectrum of ZnTPP was markedly distinct from that of ZIF-8, containing peaks at 398.6 eV (peak A), two closely spaced peaks at 400.9 and 401.7 eV (collectively referred to here as peak B), and a broader feature around 407 eV (peak C). Peak A and B originate from the excitation of a N 1s electron into antibonding π* states of the porphyrin macrocycle [34], whereas peak C can be attributed to N 1s → σ* transition [35]. For the Zn-N-C-600 sample, prepared at a pyrolysis temperature of 600 °C, peak A was observed at ~399.0 eV and peak B ~401.2 eV. We tentatively assign these to pyridinic N and pyrrolic N environments, respectively [36]. On increasing the pyrolysis temperature to 800 °C, peak A shifted to a slightly lower energy of 398.8 eV, whilst peak B (and also peak C) remained largely unshifted. The spectrum of the Zn-N-C-900 sample was qualitatively similar to that of ZnTPP, implying that porphyrin-like square planar nitrogen sites exist on the sample surface (i.e., in-plane N_4 sites). The shift in the position of peak A to lower photon energy with increasing pyrolysis temperature was of special interest, suggestive of an increase in charge transfer between Zn and N [36], which is not unexpected as the Zn atoms underwent a tetrahedral (ZIF-8-500) to near square planar (Zn-N-C-900) coordination change with increasing pyrolysis temperature.

Zn K-edge EXAFS provided detailed information about the Zn-N coordination in ZIF-8, ZIF-8-500, Zn-N-C-*T* (*T* = 600–900 °C) and ZnTPP. The Zn K-edge R-space plots for each sample are shown in Fig. 2b, whilst Zn-N scattering paths fitted to each individual spectrum are shown in Fig. S5 (online). From the fittings, Zn-N bonding distances and first shell coordination numbers were calculated (Table 1). All of the samples possess a Zn-N coordination number close to 4 (ZIF-8, CN 4.0; ZIF-8-500, CN 4.2; and Zn-N-C-*T*, CN 4.0–3.7), decreasing slightly with pyrolysis temperature in the range 600–900 °C. Results confirm a ZnN_4 configuration for all samples. For ZIF-8 and ZIF-8-500, the Zn-N bonding distances were 1.987 and 1.988 Å, typical for tetrahedrally coordinated Zn^{2+} in ZIF-8. For the Zn-N-C-600 sample, the Zn-N bond distance was much larger (Zn-N = 2.052 Å). As the pyrolysis temperature increased in the range 600–900 °C, the Zn-N distance decreased from 2.052 to 2.035 Å, the latter being comparable to the Zn-N distance in ZnTPP (2.028 Å). We attribute the shortening of the Zn-N bond distance on going from Zn-N-C-600 to Zn-N-C-900 to the formation of well-defined in-plane ZnN_4 centers at higher temperatures.

Remnants of non-planar ZnN_4 environments in the Zn-N-C-*T* samples were further evidenced by closer examination of Zn K-edge XAS spectra. In the Zn K-edge XAS spectrum of ZnTPP (Fig. 4a), no pre-edge features associated with 1s → 3d transitions were seen, consistent with Zn^{2+} in ZnTPP having a $3d^{10}$ configuration. Above the absorption edge, three main features are seen, labelled as A, B and C. Since most metal porphyrins share the same features in their K-edge XAS spectra [37], features A, B, and C in ZnTPP can be assigned with reference to FeTPPCl [38]. Feature A (9661.7 eV) is a Zn 1s to Zn $4p_z$ transition with simultaneous ligand to metal charge transfer. This feature has been identified as providing a fingerprint for in-plane MN_4, and therefore the intensity of this feature is greatly affected by the distortions from a pure square planar geometry. Feature B (9669.5 eV) results from a Zn 1s to Zn $4p_{xy}$ transition. Feature C (9672.6 eV) involves multiple scattering

Table 1
EXAFS fitting parameters at Zn K-edge for ZIF-8 and Zn-N-C-*T* pyrolysis products.

Zn-N Path	CN [a]	*R* (Å) [b]	σ^2 (10^{-3} Å^2) [c]	ΔE_0 (eV) [d]	*R* factor (%) [e]
ZIF-8	4.0(6)	1.987(15)	4.8 (2)	7 (2)	1.33
ZIF-8-500	4.2(6)	1.988(12)	4.8 (15)	6 (2)	0.98
Zn-N-C-600	4.0(2)	2.052(6)	6.3 (9)	−0.5 (6)	0.20
Zn-N-C-700	4.0(2)	2.045(6)	5.9 (9)	−0.3 (6)	0.20
Zn-N-C-800	3.8(2)	2.038(5)	6.9 (8)	−0.5 (5)	0.16
Zn-N-C-900	3.7(3)	2.035(9)	7.0 (9)	0.8 (7)	0.46
ZnTPP	3.8(4)	2.028(9)	4.1(12)	6(1)	0.64

[a] N is the coordination number; [b] *R*: interatomic distance between central atoms and surrounding coordination atoms; [c] σ^2 is Debye-Waller factor to measure thermal and static disorder in absorber-scatter distances; [d] ΔE_0: edge-energy shift (the difference between the zero kinetic energy value of the sample and that of the theoretical model); [e] *R* factor is used to value the goodness of the fitting. The number in the bracket is the last digit error.

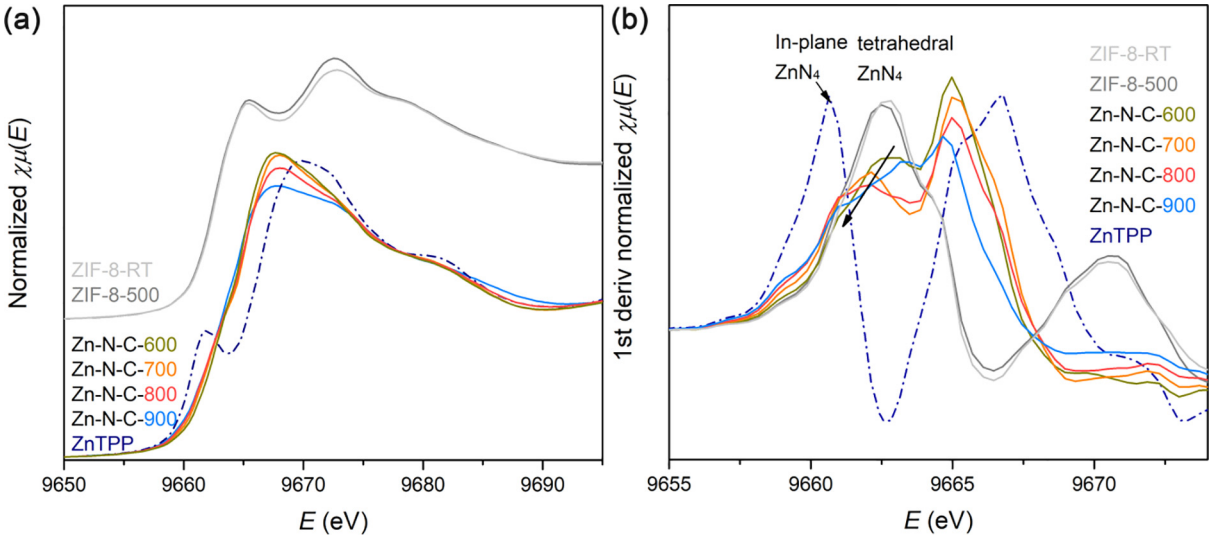

Fig. 4. (Color online) (a) Zn K-edge XAS spectra and (b) the first derivative Zn K-edge XAS spectra for ZIF-8, various Zn-N-C-*T* samples and ZnTPP.

paths, and serves as a general fingerprint of local Zn environments with different Zn-N bonding distances. Reproduction of the spectral features A, B, C requires at least five coordination shells (up to the third shell C atoms in the benzene rings of ZnTPP) [37]. In other words, any distortions from the square planar ZnN_4 geometry in ZnTPP structure would result in an energy shift or intensity change of all these features. The ZIF-8 precursor with tetrahedral ZnN_4 coordination, was naturally spectroscopically distinct from ZnTPP, showing features denoted A' and B' at 9665.0 and 9672.5 eV, respectively (involving Zn 1s → 4p transitions). Both features are similar to those reported for ZIF-7 (also tetrahedal ZnN_4) [39]. As expected, the Zn K-edge XAS spectrum of ZIF-8-500 was almost identical to that of ZIF-8, indicating a tetrahedral ZnN_4 geometry was retained in the sample.

For the Zn-N-C-600 to Zn-N-C-900 samples, the Zn K-edge XAS spectra evolved to resemble the spectrum of ZnTPP, though peak A was barely visible. The first derivative Zn K-edge spectra (Fig. 4b) show that peak A for ZnTPP appears as a weak shoulder at ~9660.6 eV in the derivative spectra for the Zn-N-C-*T* (*T* = 600–900 °C) samples, intensifying slightly with pyrolysis temperature [38]. The fact that peak A was weak for Zn-N-C-*T* (*T* = 600–900 °C) indicated that the Zn^{2+} cations were not sitting perfectly in the N_4 plane of the porphyrin-like sites. This is not surprising, given that the pyrolysis route used to prepare the Zn-N-C-*T* samples, where significant disorder is expected in the first few coordination shells around each Zn atom. The subtle variations seen in the positions and intensities of peak B and peak C (Fig. 4a) with increasing pyrolysis temperature suggest a shift in the position of Zn^{2+} closer to a square planar ZnN_4 geometry. Similar observations were made in theoretical Fe K-edge XAS studies of Fe-N_4-like catalytic centers as Fe cations approached the N_4 plane [38]. Thus, our data strongly suggest that the Zn-N-C-*T* samples (*T* = 600–900 °C) contain ZnN_4 centers, with the Zn^{2+} moving closer to the porphyrin-like N_4 plane with pyrolysis temperature up to 900 °C.

Porphyrin-like Zn sites on N-doped carbons are capable of catalysing the peroxidase-like decomposition of H_2O_2 into hydroxyl radicals (·OH). The peroxidase-like activity of ZIF-8, ZIF-8-500 and the various Zn-N-C-*T* (*T* = 600–900 °C) samples was investigated, using the colorimetric reaction of 3,3',5,5'-tetramethylbenzidine (TMB) in the presence of H_2O_2. Free hydroxyl radicals produced by the decomposition of H_2O_2 react with TMB to give a blue TMB oxidation product with a UV–vis absorbance maximum at 652 nm. At a reaction time of 30 min, the Zn-N-C-800 and Zn-N-C-900 catalysts showed very good peroxidase-like activity (Fig. 5a and Fig. S6 online). The Zn-N-C-750 sample showed modest peroxidase-like activity, whereas the Zn-N-C-700 and Zn-N-C-600 samples showed very weak peroxidase-like activity. The peroxidase-like activity of the samples followed the order Zn-N-C-800 > Zn-N-C-900 ≫ Zn-N-C-750 ≫ Zn-N-C-700 > Zn-N-C-600. No peroxidase-like activity was observed for the ZIF-8 and ZIF-8-500 catalysts.

On account of the fact that Zn-N-C-800 showed the best peroxidase-like activity, more detailed kinetic studies were performed on this sample. Similar to natural horseradish peroxidase (HRP), the activity of Zn-N-C-800 catalysts was found to depend strongly on the catalyst concentration, pH, and temperature (Figs. S7, S8 online). Fig. S7 (online) shows the activity increased with catalyst concentration (with a value of 25 μg mL^{-1} being used

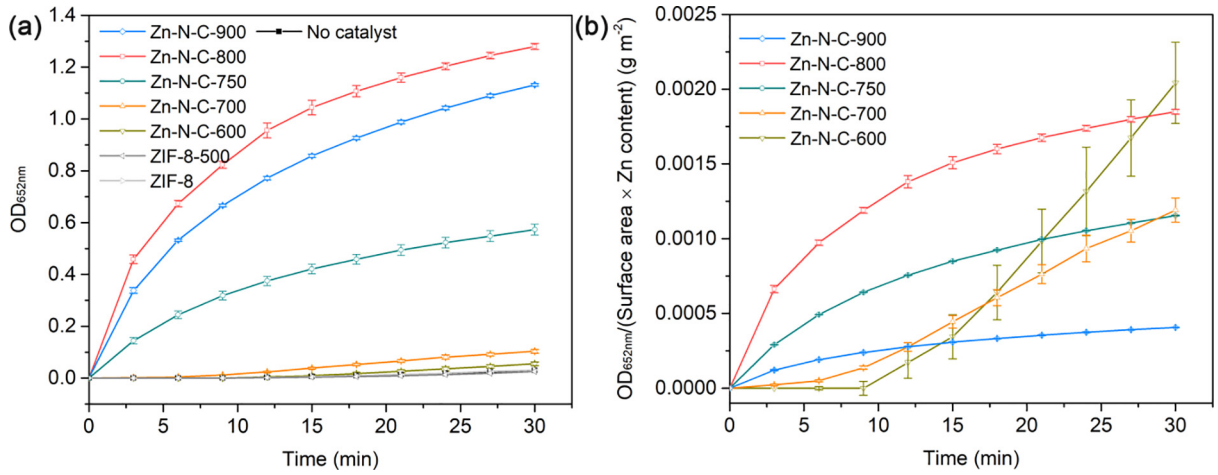

Fig. 5. (Color online) (a) Absorbance-time curves and (b) absorbance/(surface area × Zn content)-time curves for the oxidation of TMB solution by ZIF-8 and various Zn-N-C-*T* samples in the presence of H_2O_2. Reaction time: 30 min.

for subsequent tests to avoid the reaction occurring too fast). The optimal pH and temperature for the Zn-N-C-800 catalyst (Fig. S8 online) were determined to be 3–3.5 and 40–50 °C, respectively. This optimal activity window was very similar to that reported for porphyrin-like Fe-N-C materials [40]. To quantitatively probe the peroxidase-like activity of Zn-N-C-800, Michaelis–Menten kinetics studies, examining both H_2O_2 substrate concentration and TMB substrate concentration, were performed. In Michaelis-Menton analyses, the constant K_m is used to estimate the binding affinity for particular substrates, with a low K_m value indicating a strong binding affinity between the enzyme and substrates. K_m values for Zn-N-C-800 towards TMB and H_2O_2 were 0.213 and 140 mmol L^{-1}, respectively (Fig. S9, Table S3 online).

To better understand the excellent peroxidase-like activity of the Zn-N-C-800 catalyst, we synthesized a "low Zn" N-doped carbon catalyst by acid-washing Zn-N-C-800. The acid treatment involved immersing the catalyst in an aqueous 10 wt% HNO_3 solution at 60 °C for 12 h, followed by repeatedly washing with water and ethanol. This removed most of the Zn(II) atoms (the Zn content in the product was 1.20 wt% by ICP-OES, or ~1/3 the Zn content of Zn-N-C-800, Table S4 online). The "low Zn" N-doped carbon had a very low peroxidase-like activity compared to pristine Zn-N-C-800 (Fig. S10 online), whilst ZnTPP showed no activity in catalysing the oxidation reaction of TMB in the presence of H_2O_2. This indicates that a surface rich in porphyrin-like ZnN_4 centers and a semi-graphitic N-doped carbon support were both requisites for achieving a high peroxidase-like activity.

As demonstrated above, all of Zn-N-C-*T* samples contained porphyrin-like ZnN_4 centers. However, the Zn-N-C-*T* catalysts differed in their graphitic character and surface area. The degree of graphitization in the Zn-N-C-*T* sample was examined by Raman spectroscopy and C K-edge XAS. As the pyrolysis temperature increased, the Zn-N-C-*T* samples become more graphitic, as evidenced by the progressive attenuation of the amorphous carbon peak in the Raman spectra with heating up to 750 °C, thus decreasing the D/G peak ratio (Fig. S11 online). Further evidence for enhanced graphitization in the Zn-N-C-*T* samples prepared at high temperatures was found in the C K edge XAS data (Fig. S12a online), where the intensity of the C 1s → π* peak at 284.6 eV became more prominent as the pyrolysis temperature increased. Indeed, the C K-edge spectrum for Zn-N-C-900 was very similar to that collected for ZnTPP. Peak fitting of the C 1s XPS spectra for the various Zn-N-C-*T* catalysts similarly revealed that the fraction of carbon as C=C species increased with temperature (Fig. S12b, Table S5 online). The surface area of the Zn-N-C-*T* catalysts was also expected to influence their performance in the peroxidase-like activity tests, with a higher is expected to be beneficial by enabling better substrate access to active sites [41,42]. The BET surface areas of the Zn-N-C-*T* samples increase with pyrolysis temperature in the range 600 to 900 °C (Table S2 online). The enhancement seen in peroxidase-like activity on going from Zn-N-C-600 to Zn-N-C-800 thus closely matched the increased in graphitic degree and surface area of these catalysts. However, the catalytic activity of the Zn-N-C-900 sample (possessing both the highest graphitic degree and highest surface area) was inferior activity to Zn-N-C-800 sample, suggesting some additional factor was contributing to the special peroxidase-like activity of Zn-N-C-800.

Thus, to gauge the intrinsic activity of ZnN_4 sites in the Zn-N-C-*T* catalysts, the "net" activity was calculated from the overall activity by dividing the BET surface area and Zn content (Fig. 5b). Following this normalization, the activities of most of Zn-N-C-*T* catalysts became quite similar (confirming the role of both surface area and Zn content in catalyst function), with the exception being the Zn-N-C-800 catalyst whose performance remained vastly superior to the other catalysts. This indicates that the ZnN_4 sites in Zn-N-C-800 catalyst possessed high intrinsic activity. According to the Sabatier principle [43], an optimal adsorption energy between the catalyst and intermediates is essential for the overall reaction to proceed efficiently. Previous studies have shown that the adsorption of H_2O_2 on MN_4 sites to form a five coordinated metal site is the rate determining step for the catalytic decomposition of H_2O_2 [21]. It is therefore intuitive that the ZnN_4 sites in Zn-N-C-800 facilitated the formation of such an intermediate, thus benefitting the peroxidase-like activity. The electron-donating ability of the support, and the position of the Zn(II) atoms with respect to the N_4 plane of the porphyrin-like sites, controls the electron density on the Zn(II) active sites [44]. These were likely the key factors in the special activity of Zn-NC-800 (resulting in optimal adsorption of H_2O_2 or an intermediate in the decomposition of H_2O_2, such as a HOO-ZnN_4 moiety) [5]. Our catalysis results suggest that as the pyrolysis temperature of the ZIF-8 precursor was increased in the range 600 to 900 °C, the electron density on the central Zn atoms increased, with the electron density on Zn(II) atoms in the Zn-N-C-800 catalyst being optimal for Zn-O binding and thus H_2O_2 adsorption and decomposition. However, as the Zn cations moved completely into the ZnN_4 plane, the electron density on Zn(II) atoms in Zn-N-C-900 catalyst became too high (unfavourable for intermediate adsorption), thus decreasing performance. We hypothesize that the electron density of the central Zn(II) atoms

in the Zn-N-C-*T* catalysts thus controls overall peroxidase-like activity.

4. Conclusion

The evolution of porphyrin-like ZnN_4 centers during the pyrolysis of ZIF-8 at temperatures ranging from 500 to 900 °C was systematically investigated. Results show that square planar porphyrin-like ZnN_4 sites were formed on N-doped carbon supports at ZIF-8 pyrolysis temperatures as low as 600 °C, with the Zn(II) atoms moving closer to the N_4 plane as the pyrolysis temperature was increased. The graphitic carbon content in the support controlled the electron density of the Zn(II) sites. The Zn-N-C-800 catalyst prepared at 800 °C offered excellent peroxidase-like activity, due to an optimal bond strength being realized for H_2O_2 adsorption on ZnN_4 sites. This work offers valuable insights for the synthesis of M-N-C materials from MOF precursors, whilst drawing researcher attention to the importance of the planarity of the MN_4 sites in efficient metal single atom catalysis.

Conflict of interest

The authors declare that they have no conflict of interest.

Acknowledgments

This work was supported by the Ministry of Business, Innovation and Employment Catalyst Fund (MAUX 1609), the University of Auckland Faculty Research Development Fund, the MacDiarmid Institute for Advanced Materials and Nanotechnology, and a generous philanthropic donation from Greg and Kathryn Trounson. Qing Wang thanks the MacDiarmid Institute for Advanced Materials and Nanotechnology for the award of a doctoral scholarship.

Author contributions

Qing Wang and Geoffrey I.N. Waterhouse conceived the experiments. Qing Wang prepared the catalysts and conducted most of the sample characterization. Toshiaki Ina assisted the EXAFS data collection and data fitting. Wan-Ting Chen participated in the XAS data collection. Lu Shang helped interpret the peroxidase-like catalytic data. Fanfei Sun assisted with XAFS data analysis. Shanghai Wei helped the HRTEM and dark-field TEM image collection. Dongxiao Sun-Waterhouse, Shane G. Telfer, Tierui Zhang and Geoffrey I.N. Waterhouse supervised Ph.D. candidate Qing Wang. All authors made worthwhile contributions to technical discussions and manuscript writing.

Appendix A. Supplementary materials

Supplementary materials to this article can be found online at https://doi.org/10.1016/j.scib.2020.06.020.

References

[1] Guo JJ, Huo JJ, Liu Y, et al. Nitrogen-doped porous carbon supported nonprecious metal single-atom electrocatalysts: from synthesis to application. Small Methods 2019;3:1900159–233.
[2] Peng Y, Lu BZ, Chen SW. Carbon-supported single atom catalysts for electrochemical energy conversion and storage. Adv Mater 2018;30:1801995–2025.
[3] Yang H, Shang L, Zhang Q, et al. A universal ligand mediated method for large scale synthesis of transition metal single atom catalysts. Nat Commun 2019;10:4585–9.
[4] Jiang K, Back S, Akey AJ, et al. Highly selective oxygen reduction to hydrogen peroxide on transition metal single atom coordination. Nat Commun 2019;10:3997–4011.
[5] Pan Y, Chen Y, Wu K, et al. Regulating the coordination structure of single-atom Fe-N_xC_y catalytic sites for benzene oxidation. Nat Commun 2019;10:4290–311.
[6] Zhang JT, Zhang M, Zeng Y, et al. Single Fe atom on hierarchically porous S, N-codoped nanocarbon derived from porphyra enable boosted oxygen catalysis for rechargeable Zn-air batteries. Small 2019;15:1900307–11.
[7] Yuan K, Lützenkirchen-Hecht D, Li L, et al. Boosting oxygen reduction of single iron active sites via geometric and electronic engineering: nitrogen and phosphorus dual coordination. J Am Chem Soc 2020;142:2404–12.
[8] Liu MM, Wang LL, Zhao KN, et al. Atomically dispersed metal catalysts for the oxygen reduction reaction: synthesis, characterization, reaction mechanisms and electrochemical energy applications. Energy Environ Sci 2019;12:2890–923.
[9] Jiao L, Jiang H-L. Metal-organic-framework-based single-atom catalysts for energy applications. Chem 2019;5:786–804.
[10] Chen Y-Z, Zhang R, Jiao L, et al. Metal–organic framework-derived porous materials for catalysis. Coord Chem Rev 2018;362:1–23.
[11] Sharifi T, Gracia-Espino E, Chen A, et al. Oxygen reduction reactions on single- or few-atom discrete active sites for heterogeneous catalysis. Adv Energy Mater 2019:1902084.
[12] Zhu Y, Sokolowski J, Song X, et al. Engineering local coordination environments of atomically dispersed and heteroatom-coordinated single metal site electrocatalysts for clean energy-conversion. Adv Energy Mater 2019:1902844–929.
[13] Yin P, Yao T, Wu Y, et al. Single cobalt atoms with precise N-coordination as superior oxygen reduction reaction catalysts. Angew Chem 2016;55:10800–5.
[14] Wang X, Chen Z, Zhao X, et al. Regulation of coordination number over single Co sites: triggering the efficient electroreduction of CO_2. Angew Chem 2018;57:1944–8.
[15] Wang J, Huang Z, Liu W, et al. Design of N-coordinated dual-metal sites: a stable and active Pt-free catalyst for acidic oxygen reduction reaction. J Am Chem Soc 2017;139:17281–4.
[16] Wang XX, Cullen DA, Pan YT, et al. Nitrogen-coordinated single cobalt atom catalysts for oxygen reduction in proton exchange membrane fuel cells. Adv Mater 2018;30:1706758–811.
[17] Wei S, Li A, Liu JC, et al. Direct observation of noble metal nanoparticles transforming to thermally stable single atoms. Nat Nanotechnol 2018;13:856–61.
[18] Yang J, Qiu Z, Zhao C, et al. *In situ* thermal atomization to convert supported nickel nanoparticles into surface-bound nickel single-atom catalysts. Angew Chem 2018;57:14095–100.
[19] Li J, Zhang H, Samarakoon W, et al. Thermally driven structure and performance evolution of atomically dispersed FeN_4 sites for oxygen reduction. Angew Chem 2019;58:18971–80.
[20] Li J, Jiao L, Wegener E, et al. Evolution pathway from iron compounds to $Fe_1(II)$-N_4 sites through gas-phase iron during pyrolysis. J Am Chem Soc 2020;142:1417–23.
[21] Xu B, Wang H, Wang W, et al. A single-atom nanozyme for wound disinfection applications. Angew Chem Int Ed 2019;58:4911–6.
[22] Yang Q, Yang CC, Lin CH, et al. Metal-organic-framework-derived hollow N-doped porous carbon with ultrahigh concentrations of single Zn atoms for efficient carbon dioxide conversion. Angew Chem 2019;58:3511–5.
[23] Yang H, Bradley SJ, Chan A, et al. Catalytically active bimetallic nanoparticles supported on porous carbon capsules derived from metal–organic framework composites. J Am Chem Soc 2016;138:11872–81.
[24] Yang H, Bradley SJ, Wu X, et al. General synthetic strategy for libraries of supported multicomponent metal nanoparticles. ACS Nano 2018;12:4594–604.
[25] Yang H, Chen X, Chen WT, et al. Tunable synthesis of hollow metal-nitrogen-carbon capsules for efficient oxygen reduction catalysis in proton exchange membrane fuel cells. ACS Nano 2019;13:8087–98.
[26] Gu J, Hsu C-S, Bai L, et al. Atomically dispersed Fe^{3+} sites catalyze efficient CO_2 electroreduction to CO. Science 2019;364:1091–4.
[27] Zhao C, Dai X, Yao T, et al. Ionic exchange of metal-organic frameworks to access single nickel sites for efficient electroreduction of CO_2. J Am Chem Soc 2017;139:8078–81.
[28] Li J, Chen M, Cullen DA, et al. Atomically dispersed manganese catalysts for oxygen reduction in proton-exchange membrane fuel cells. Nat Catal 2018;1:935–45.
[29] Luo E, Zhang H, Wang X, et al. Single-atom Cr-N_4 sites designed for durable oxygen reduction catalysis in acid media. Angew Chem Int Ed 2019;58:12469–75.
[30] Qu Y, Li Z, Chen W, et al. Direct transformation of bulk copper into copper single sites via emitting and trapping of atoms. Nat Catal 2018;1:781–6.
[31] Xiao M, Gao L, Wang Y, et al. Engineering energy level of metal center: Ru single-atom site for efficient and durable oxygen reduction catalysis. J Am Chem Soc 2019;141:19800–6.
[32] Xiao M, Zhu J, Li G, et al. A single-atom iridium heterogeneous catalyst in oxygen reduction reaction. Angew Chem Int Ed 2019;58:9640–5.
[33] Kroll T, Kraus R, Schönfelder R, et al. Transition metal phthalocyanines: insight into the electronic structure from soft X-ray spectroscopy. J Chem Phys 2012;137:054306.
[34] Sivkov VN, Zabrodina GS, Nekipelov SV, et al. NEXAFS study of zinc porphyrins intercalated into V_2O_5 xerogel. Macroheterocycles 2011;4:213–5.
[35] Zhong J, Deng J-J, Mao B-H, et al. Probing solid state N-doping in graphene by X-ray absorption near-edge structure spectroscopy. Carbon 2012;50:335–8.

[36] Tong Y, Chen P, Zhou T, et al. A bifunctional hybrid electrocatalyst for oxygen reduction and evolution: cobalt oxide nanoparticles strongly coupled to B,N-decorated graphene. Angew Chem 2017;56:7121–5.
[37] Rossi G, d'Acapito F, Amidani L, et al. Local environment of metal ions in phthalocyanines: K-edge X-ray absorption spectra. Phys Chem Chem Phys 2016;18:23686–94.
[38] Jia Q, Ramaswamy N, Hafiz H, et al. Experimental observation of redox-induced Fe-N switching behavior as a determinant role for oxygen reduction activity. ACS Nano 2015;9:12496–505.
[39] Goesten M, Stavitski E, Pidko EA, et al. The molecular pathway to ZIF-7 microrods revealed by in situ time-resolved small- and wide-angle X-ray scattering, quick-scanning extended X-ray absorption spectroscopy, and DFT calculations. Chem 2013;19:7809–16.
[40] Jiao L, Xu W, Yan H, et al. Fe-N-C single-atom nanozymes for the intracellular hydrogen peroxide detection. Anal Chem 2019;91:11994–9.
[41] Xue T, Jiang S, Qu Y, et al. Graphene-supported hemin as a highly active biomimetic oxidation catalyst. Angew Chem 2012;51:3822–5.
[42] Sun H, Zhou Y, Ren J, et al. Carbon nanozymes: enzymatic properties, catalytic mechanism, and applications. Angew Chem 2018;57:9224–37.
[43] Sabatier P. Hydrogenation and dehydrogenation by catalysis. Ber Dtsch Chem Ges 1911;44:1984–2001.
[44] Ramaswamy N, Tylus U, Jia Q, et al. Activity descriptor identification for oxygen reduction on nonprecious electrocatalysts: linking surface science to coordination chemistry. J Am Chem Soc 2013;135:15443–9.

Qing Wang received her M.S. degree in Materials Science from the University of Chinese Academy of Sciences. Currently, she is a Ph.D. candidate at the University of Auckland, New Zealand, under the supervision of Professor Geoffrey Waterhouse. Her research focuses on the development of non-precious metal catalysts and electrocatalysts for energy conversion and other applications.

Geoffrey I. N. Waterhouse completed a Ph.D. degree in Chemistry at the University of Auckland in 2003. Currently he is the Energy Theme leader in the MacDiarmid Institute for Advanced for Advanced Materials and Nanotechnology (a New Zealand Centre of Research Excellence), and a Chair Professor of both the South China University of Technology and Shandong Agricultural University. His research interest includes solar energy capture technologies, photocatalysis, photonic band gap materials, and biosensors.